Design and Experimental Validation of a Novel High-Speed Omnidirectional Underwater Propulsion Mechanism

Taylor Njaka, *Graduate Student Member, IEEE*, Stefano Brizzolara, and Pinhas Ben-Tzvi, *Senior Member, IEEE*

***Abstract*—This article details the design, working principles, and testing of a novel position control mechanism for marine operations or inspection in extreme, hostile, or high-speed turbulent environments where unprecedented speed and agility are necessary. The omnidirectional mechanism consists of a set of counter-rotating blades operating at frequencies high enough to dampen vibrational effects on onboard sensors. Each rotor is individually powered to allow for roll control via relative motor effort and attached to a servo-swashplate mechanism, enabling quick and powerful manipulation of fluid flow direction in the hull's coordinate frame without the need to track rotor position. The mechanism inherently severs blade loads from servo torques, putting all load on the main motors and minimizing servo response time, while exploiting consistent blade momentum to minimize the corresponding force response time. A small-scale force-validating model is fabricated and tested for various force and moment commands. Kinematic and hydrodynamic analyses of the hull and surrounding fluid forces during various blade maneuvers are presented, followed by the mechanical design and kinematic analysis of each subsystem in a small scale model. Experimental results of the small-scale model are presented that verify the concepts presented for the larger-scale model. Finally, an open-loop controller is constructed with decoupled parameters for each degree of freedom.**

***Index Terms*—AUV, high-speed remotely operated vehicle (ROV), omnidirectional propulsion, unmanned underwater vehicle (UUV), underwater rotorcraft.**

I. Introduction

Long has there been a divide between the class of submersibles composed of streamlined, torpedo-shaped vehicles autonomous underwater vehicles (AUVs) and that of omnidirectional or semiomnidirectional crafts resembling the famous *ALVIN* submersible remotely operated vehicles (ROVs). Crafts such as the latter are capable of complex tasks involving external manipulation but are lethargic in nature and prone to flow-based disturbances, as found in shallow waters at stormy conditions or in turbulent tidal environments near artificial piers. There exists a need for an unmanned underwater vehicle (UUV) which combines the speed and agility of AUVs with the full-omnidirectionality and precision of ROVs [1]–[3]. Such a vehicle could potentially operate in conditions unreachable to the other two vehicle classes, while reducing the total operating time and thereby the financial and strategic cost for deployment in ROV-specific applications.

The growing interest in robots replacing humans in turbulent, potentially dangerous environments [4] where precision, speed, and robustness are necessary [5] has inspired the development of a new class of underwater robotic thrust mechanism capable of true agile omnidirectionality in a compact design. Fig. 1 outlines the mechanism. Challenges include but are not limited to minimizing reaction time to position disturbances, which is hindered by the delay of accelerating water and the thrust-to-mass ratio of any smaller craft attempting to actively reject disturbance. For large crafts, resilience to disturbances is inherent in vehicle mass, but fast position control is not practical. In much smaller crafts, fast position control is possible but delayed by the acceleration time of traditional ducted thrusters, making their inherent susceptibility to disturbances difficult to overcome.

Classifying the proposed design with AUVs or ROVs is largely subjective. Traditional AUVs are high-speed, underactuated flight vehicles used primarily for underwater mapping and survey applications. Omnidirectional ROVs, on the other hand, are used primarily for inspection and intervention. Like the proposed design, ROVs share the same zero-turning radius benefit that results from their omnidirectionality, but suffer greatly in maximum speed and agility, where *agility* can be measured as the potential for instantaneous acceleration on demand. This is quantified by dividing maximum thrust by the sum of mass and added mass, where *added mass* is the virtual added mass created by fluid momentum around an accelerating body. The proposed design possesses the speed capabilities of traditional AUVs while maintaining the zero-turning radius of omnidirectional

Manuscript received September 30, 2020; accepted November 7, 2020. Recommended by Technical Editor J. Liu and Senior Editor Y. Li. *(Corresponding author: Taylor Njaka.)*

Taylor Njaka and Pinhas Ben-Tzvi are with the Department of Mechanical Engineering, Virginia Tech, Blacksburg, VA 24061 USA (e-mail: njaka@vt.edu; bentzvi@vt.edu).

Stefano Brizzolara is with the Kevin T. Crofton Department of Aerospace and Ocean Engineering, Virginia Tech, Blacksburg, VA 24061 USA (e-mail: stebriz@vt.edu).

This article has supplementary material provided by the authors and color versions of one or more figures available at https://doi.org/10.1109/TMECH.2020.3037887.

Digital Object Identifier 10.1109/TMECH.2020.3037887

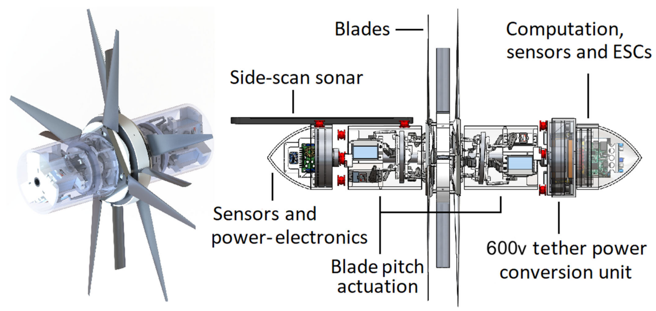

Fig. 1. **(Left)** Propulsion mechanism. **(Right)** UUV implementation with displacement 10.81 kg and total vehicle length 0.86 m.

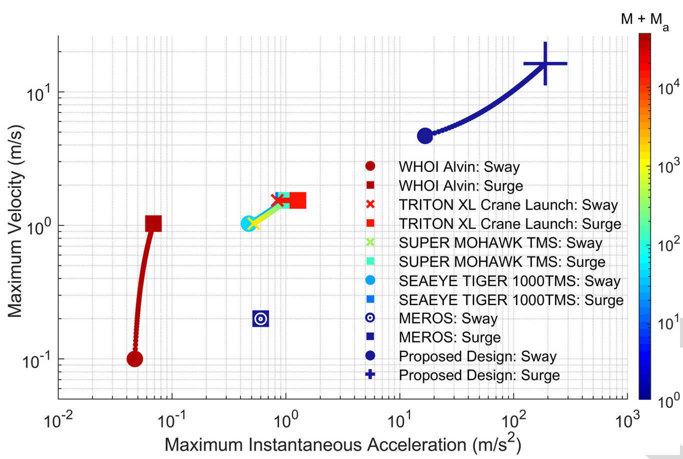

Fig. 2. Comparison of mass, top speed, and agility-based characteristics of typical ROVs with proposed design.

ROVs [6]. With its omnidirectionality and ability to carry and manipulate a payload, the proposed system is perhaps better classified with ROVs. Its high power consumption also bolsters this classification [7], as it would require a tether for missions exceeding 15 minutes.

Fig. 2 compares *mass + added mass, top speed,* and *agility* of typical omnidirectional ROVs [8]–[10] with the proposed design characteristics. Added masses are calculated from vehicle geometries [11], [12] and virtual planar-motion mechanism tests [13]. For completeness, a wide range of ROVs is considered ranging from *heavy work-class* ROVs to *observation-class* ROVs in the size range of the proposed system. The ROV-profiled *Alvin* is also included for reference.

One small-profile omnidirectional ROV, the *MEROS* [14], attempts to achieve adequate agility by maximizing thrust and minimizing size, but limitations using this method are realized as the craft's very thrusters greatly impact its final volume and shape profile. A CAD representation of the MEROS is shown in Fig. 3.

The proposed design decouples blade-pitch actuator loads from rotor torques and forces while exploiting properties of already-moving water to eliminate the delay between actuator action and force output [6]. Such high agility and reaction time may allow the craft to not only *react to* but actively *reject* various

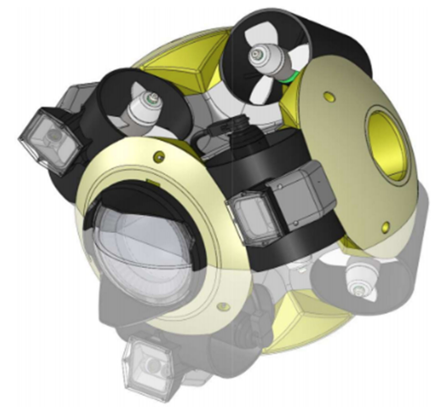

Fig. 3. [14] CAD representation of the *MEROS* ROV. With a diameter of 0.4 m, the MEROS is similar in size to the proposed design, which has a length of 0.406 m without nose attachments.

types of disturbances. Modeling said rejections are outside the scope of this study and reserved for future work.

The ability for the proposed craft to vector thrust within its low profile and still control tremendous power may allow it to achieve exceptional maneuverability, but the concept must first be tested. The purpose of this study is to demonstrate the dynamic thrust ability of the novel omnidirectional thrust mechanism through physical small-scale experimentation.

For clarity, a previous conference paper by the authors [6] presented simplified CFD simulation data on the proposed full-scale UUV design, to merely shed light on the operating theory. As critical background information, this current study revisits the mechanism's complex working principles and mentions theorized full-scale performance. It does not detail previously published engineering designs, methods, or results.

This article instead focuses on a different fully fabricated small-scale proof-of-concept for validating the working principles behind the proposed theoretical UUV equipped with our mechanism, as the mechanism's hydrodynamic complexity calls for physical experimentation for any noteworthy validation. The small-scale proof-of-concept prototype was built specifically for this study and is presented for the first time in this article. The small-scale model is designed only for static force-readings, in stark contrast to the proposed full-scale dynamic model presented in the previous study. Both models are designed around Bullard Pull conditions for omnidirectionality, as they are expected to be equally responsive along any two opposite directions. They both share the same mechanism. This study aims to prove the mechanism's rationality as a whole through experimental comparison with the hypothesis. Any findings presented in this study are entirely novel, and we believe the results to be significant.

II. Working Principles

We propose a small craft capable of true omnidirectionality at high speeds. The proposed design utilizes two decoupled counter-rotating rotors, each consisting of four highly actuated blades centered around a hollow tubing framework. The central

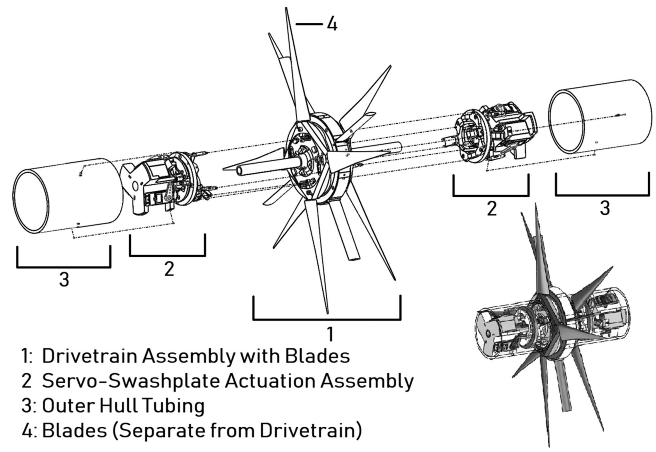

Fig. 4. Overview of all full-scale model sub-assemblies.

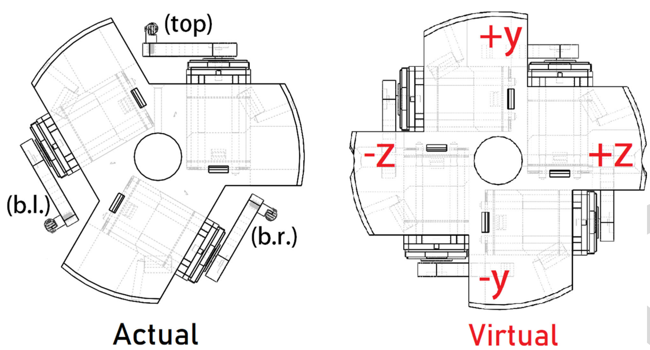

Fig. 5. Servo alignment for swashplate actuation.

tubing network is chosen to allow for the safe wiring of four 670-W brushless motors operating at maximum load. The hull is intended to be largely free-flowing for required motor cooling and quick deployment. Such cooling is made necessary by the considerable power-to-volume ratio of the motors, enabling the craft to produce upwards up 2500 N on its primary axis [6]. Designed mostly around premanufactured parts, the outer hull has a main diameter of 0.14 m and length of 0.41 m without nose attachments. Fig. 4 presents an overview of the full-scale design.

Each of the two rotors contains one servo-swashplate actuation mechanism (SSPAM), which must quickly manipulate the pitch of spinning blades in a passive controlled manner, independent of the rotation rate. This is realized by using three servos to alter the planar projection of a wide bearing assembly (swashplate) connected to the trailing edge of each blade. For explanation purposes, we will assume each SSPAM is actually composed of $four$ servos: +y, -y, +z, and -z, as shown in Fig. 5.

The virtual four-servo-per-rotor model greatly facilitates control-command implementation. Each servo in a rotor directly controls the pitch of blades passing through its particular quadrant, and all four servos are given the same forward offset parameter. A top servo (+y) controls the pitch of all blades passing through its (top) quadrant. A bottom servo (-y) controls the pitch of all blades passing through the bottom quadrant, while the difference between the two controls the relative thrust effort between top and bottom quadrants, thus controlling the yaw-related moment across the hull itself. The shared forward offset between these servos +y and -y directly controls the net forward thrust of all blades passing through quadrants +y and y. When the same forward offset is applied to all four blades, it is an adequate control for overall surge thrust, as thrust is linear with blade pitch in our angle range and can therefore be superimposed. Physical servo-arm and blade-pivot geometries are chosen for blade angles to match corresponding actuator angles in a four-servo configuration. The four-servo plate-control model is trivially realized back to the three-servo model with a simple transformation, where the three servos are labeled (top), (b.r.), and (b.l.)

$$\begin{aligned}
&\angle(top) = \angle(+y)\\
&\angle(b.r.) = \frac{1-\sqrt{3}}{4}\angle(+y) + \frac{3-\sqrt{3}}{4}\angle(-y) + \frac{\sqrt{3}}{2}\angle(+z)\\
&\angle(b.l.) = \frac{1-\sqrt{3}}{4}\angle(+y) + \frac{3-\sqrt{3}}{4}\angle(-y) + \frac{\sqrt{3}}{2}\angle(-z)
\end{aligned} \tag{1}$$

where (top) represents the uppermost servo, $(b.r.)$ represents the bottom right servo, and $(b.l.)$ represents the bottom left servo in a triangular orientation. A four-servo controller would use this transformation to output appropriate values to servos in the physical three-servo model.

The four-servo-per-rotor model also allows for decoupled bi-planar control and intuitive two-dimensional Cartesian controller representation. Because all four servos are fed with the same forward offset surge-command, servos ±z can control the craft's behavior in the horizontal plane while servos ±y control the craft's behavior in the vertical plane. Furthermore, any subsequent horizontal-plane control parameter that is fed to servo +z as a value N will be fed to servo -z as the value -N. The same holds true for servos ±y. Notice how the centroid of the swash plate connecting the four servos never shifts for such control inputs, completely decoupling inputs unique to the *xy* plane from inputs unique to the *xz* plane. A two-dimensional representation can then be constructed that depicts how the vehicle behaves in the isolated *xy* plane. Viewing the entire hull from the side, we explore the interactions between virtual actuators ±y on the ±x rotors during different maneuvers. Fig. 6 illustrates the two-dimensional surge maneuver in Cartesian space.

Likewise, Fig. 7(a) illustrates the yaw maneuver in two dimensions and specifies control inputs governed by global vertical yaw parameter β. Yaw inputs -β, β, -β, and β are fed directly to servos 1, 2, 3, and 4, respectively. Control parameters can be superimposed to achieve multiple maneuvers simultaneously, as they do not inherently interfere with each other [15] due to the rigid nature of the blades. Fig. 7(b) details how control parameters α and β would be fed to servos 1-4 to execute two independent control modes at once.

A third control parameter Γ is proposed for sway. Such a maneuver is made possible from the rigid nature of the blades and durable alignment-locking of the rotor axes. As with the other planar control parameters, sway-related actuator inputs do

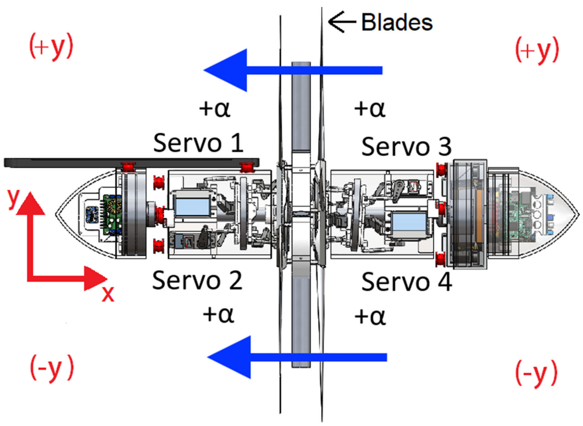

Fig. 6. 2-D surge maneuver on a full ROV implementation. Surge parameter α is fed to all servos in the proposed design, causing a positive thrust in $\hat{x}$. The resulting flow is represented with blue arrows.

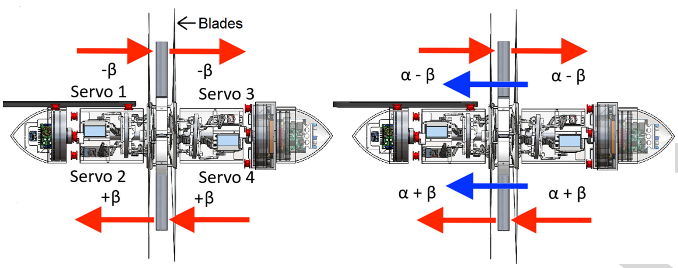

Fig. 7. (a, left) 2-D yaw maneuver on ROV implementation. (b, right) 2-D superposition of yaw and surge maneuvers. Servos are fed the summation of different control parameters. Arrows conceptualize components of the fluid flow resulting from commands α and β.

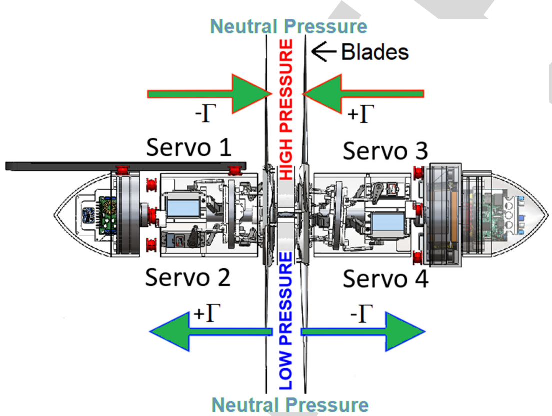

Fig. 8. 2-D sway maneuver on ROV implementation. Sway parameters -Γ, Γ, Γ, and -Γ are added to servo inputs 1, 2, 3, and 4, respectively.

not shift swashplate centroids, maintaining isolation between all vertical and horizontal-plane maneuvers. The lack of kinematic overlap allows for superposition of *all* control parameters, as they do not fundamentally interfere with each others' functionality [15]. Fig. 8 elaborates on the principle behind the sway maneuver mechanism.

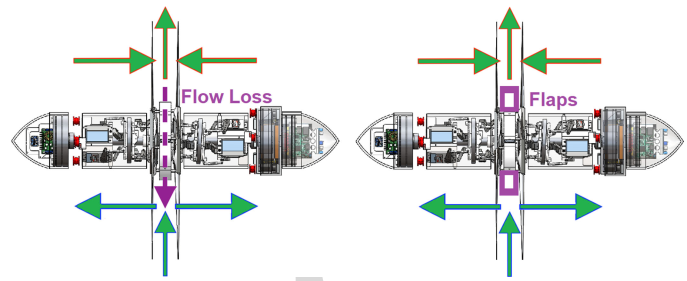

Fig. 9. Flow loss due to pressure differential across space between rotors. Unwanted flows are minimized through the *BARFA* flaps described in Section III-A.

Flow leakage between the high and low pressure regions would reduce sway thrust. The issue regarding unwanted flow across the pressure differential in the sway maneuver is presented and solved in Fig 9.

Final inputs to virtual servos 1–4 are then, respectively, α-β-Γ, $\alpha+\beta+\Gamma$, α-$\beta+\Gamma$, and $\alpha+\beta$-Γ. We set $\alpha \in (-10^o, 10^o)$, $\beta \in (-10^o, 10^o)$, and $\Gamma \in (-10^o, 10^o)$ such that $|\alpha+\beta+\Gamma| < 30^o$, the physical control limit of each servo. Servo arm and blade pivot lengths are chosen to match blade angles with servo angles in corresponding quadrants.

Rotors are decoupled from one-another to allow for simple roll control via torque-balancing. Because the effective input to each rotor is torque, not speed, roll-torque remains balanced regardless of blade parameters and relative speed, as the rotation rate is simply a byproduct of the torque input. This allows for roll control via a single parameter δ, effectively decoupled from all other parameters and realized merely by varying the relative effort between the two rotors. The separate rotors are read 90% effort $\pm\delta$, where $\delta \in (-10\%, 10\%)$. Control parameters are then mapped to physical actuator commands as follows:

$$\begin{bmatrix} +x \text{ Rotor Effort} \\ -x \text{ Rotor Effort} \\ +x \text{ ``}top\text{''Servo Angle} \\ +x \text{ ``}b.r.\text{''Servo Angle} \\ +x \text{ ``}b.l.\text{''Servo Angle} \\ -x \text{ ``}top\text{''Servo Angle} \\ -x \text{ ``}b.r.\text{'' Servo Angle} \\ -x \text{ ``}b.l.\text{''Servo Angle} \end{bmatrix} = \begin{bmatrix} 90\% \\ 90\% \\ 90^o \\ 90^o \\ 90^o \\ 90^o \\ 90^o \\ 90^o \end{bmatrix}$$

$$+ \begin{bmatrix} 0 & 0 & 0 & -1 & 0 & 0 \\ 0 & 0 & 0 & 1 & 0 & 0 \\ 1 & 0 & -1 & 0 & -1 & 0 \\ 1 & \frac{\sqrt{3}}{2} & \frac{1}{2} & 0 & \frac{1}{2} & -\frac{\sqrt{3}}{2} \\ 1 & -\frac{\sqrt{3}}{2} & \frac{1}{2} & 0 & \frac{1}{2} & \frac{\sqrt{3}}{2} \\ -1 & 0 & -1 & 0 & 1 & 0 \\ -1 & -\frac{\sqrt{3}}{2} & \frac{1}{2} & 0 & \frac{-1}{2} & -\frac{\sqrt{3}}{2} \\ -1 & \frac{\sqrt{3}}{2} & \frac{1}{2} & 0 & \frac{-1}{2} & \frac{\sqrt{3}}{2} \end{bmatrix} \begin{bmatrix} \alpha \\ \Gamma_y \\ \Gamma_z \\ \delta \\ \beta_y \\ \beta_z \end{bmatrix} \tag{2}$$

where Γ_y and Γ_z, respectively, control force along $\hat{y}$ and $\hat{z}$, while β_y and β_z, respectively, control moment about $\hat{y}$ and $\hat{z}$. Fig. 10

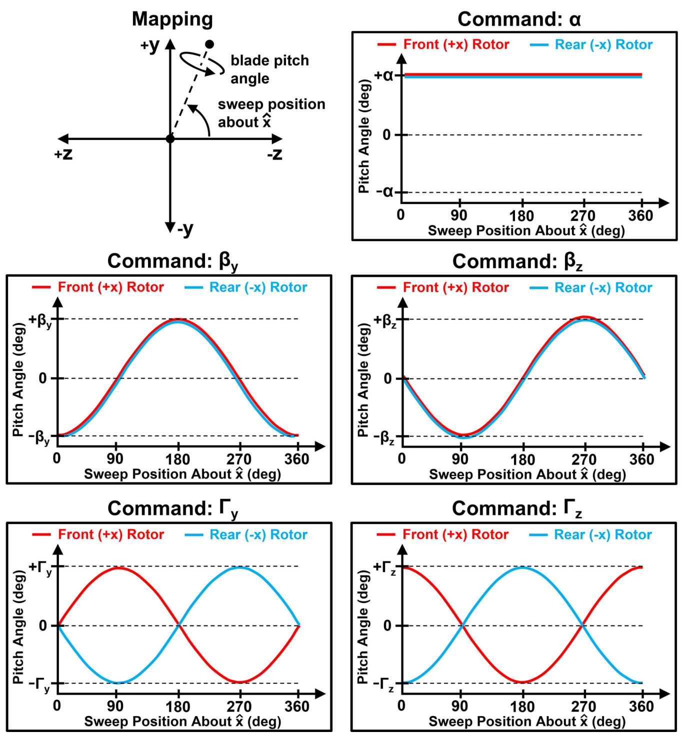

Fig. 10. Blade pitch angles throughout the sweep.

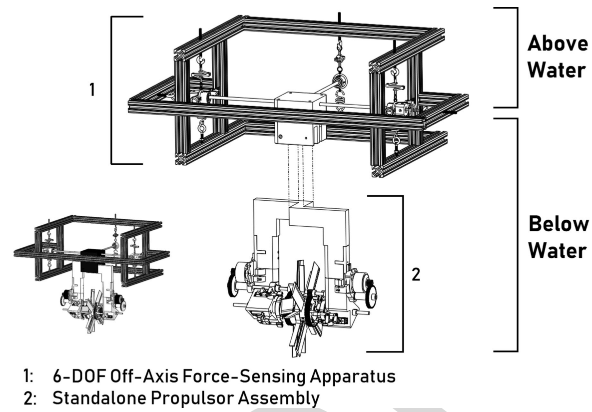

Fig. 11. Test setup of the small-scale model.

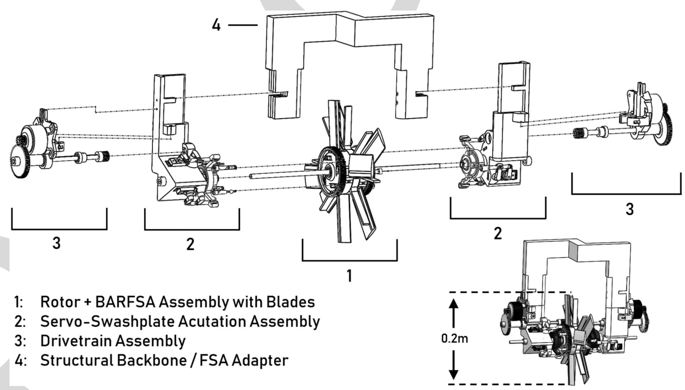

Fig. 12. Subcomponents of the small-scale propulsor.

shows how the blades alter pitch during their sweep about $\hat{x}$, in response to each superimposable control parameter.

It is important to note that the conceptual validation of roll, surge, and yaw maneuvers was determined to have lesser relevance in testing the practicality of the proposed mechanism. For example, in no reasonable scenario will pulling *all* blade pitches forward *not* cause the craft to surge as intended if properly programmed with servo limits considered. Yaw and roll control parameters are similarly straightforward. These maneuvers are practically identical to the operational foundation of all dual-blade rotorcraft [15]. The omnidirectionality of the proposed mechanism comes from its unique ability to potentially *sway* quickly, allowing it to move in any orientation at speeds far beyond the scope of ROVs or AUVs. STARCCM+ computational fluid dynamic (CFD) simulations suggest the propulsor can generate sway thrust at a magnitude near 10–20% surge thrust capability [6]. A small-scale physical model is then constructed to both validate the dynamic omnidirectional thrust ability of the craft, and gauge the feasibility of the novel sway maneuver as a principle.

III. Small-Scale Model Design

A small-scale force-validation model was constructed to verify the conceptual working principles. The model was designed to be tested in a water tank while fixed to an off-axis, 6-DOF force-sensing apparatus placed above the tank. The experimental testing tank setup is outlined in Fig. 11.

The force-sensing apparatus is designed and fabricated economically using 80/20 aluminum bars to measure any forces and moments imposed by the attached propulsor at a depth of 0.3 m in bullard pull. The sensor configuration and operating principles of the apparatus are not covered in this study, which focuses on the design and performance of the propulsor itself. An overview of the standalone small-scale propulsor assembly is shown in Fig. 12.

Because the small-scale force-validation model is never intended to physically accelerate, the overall design process is simplified, allowing the small-scale model to be economical and predominantly 3-D printed without mass-related limitations. Design emphasis is now focused primarily on clearing space around the rotating blades rather than compacting and streamlining the entire subassembly area. Unlike in the full-scale model, small-scale subassemblies are then encouraged to be placed much further from the dynamic rotors, greatly simplifying the design as a whole.

A. Drivetrain and Rotor Mechanism

In the drivetrain mechanism, for example, the motors and obtrusive gears are as far away from the dynamic rotors as possible so as to not disrupt the generated forces and moments. The drivetrain must provide independent torque to each rotor while locking relative rotor alignment and be able to support the stationary flaps responsible for limiting unwanted flow. Fortunately, geometric exploits allow for a relatively simple

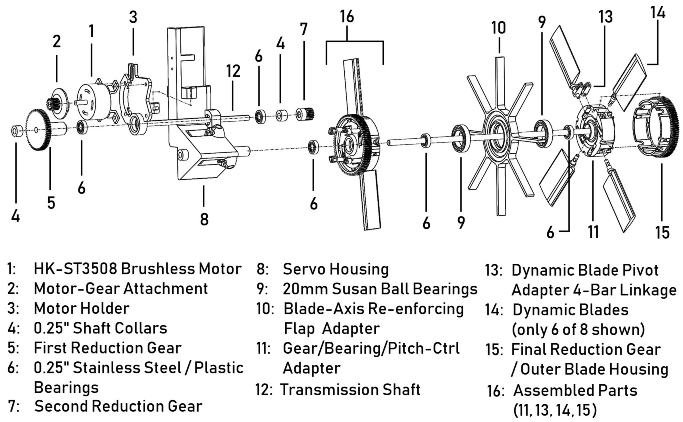

Fig. 13. Small-scale drivetrain and rotor assembly.

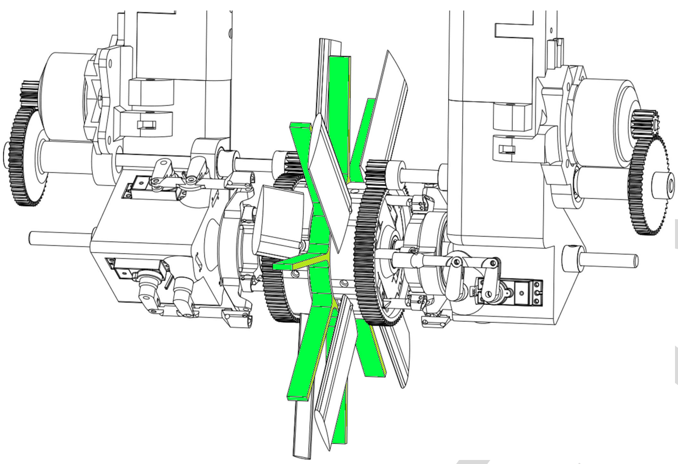

Fig. 14. BARFA mechanism for eliminating unwanted fluid flow and securing rotor alignment (highlighted).

design solution. An engineering diagram of the entire drivetrain mechanism is shown in Fig. 13.

The drivetrain on each rotor is powered by a Hobbyking ST3508-730kv brushless motor. These inexpensive motors are chosen for their exceptional torque, power, size, and material-based bearing design which allows for corrosion resistance uncommon for motors of their size. Their significant torque output ($\geq$1.1 N-m stall) is aided by a further 15:1 gear reduction in the drivechain. With the rotors spanning only 0.2 m total diameter, we expect minimal rotation rate loss due to the drag from the blades alone. Fluid compression and churning losses on the submerged gearing [16], [17], especially at the motor location, are expected to have the largest influence on rotation rate drop.

To prevent unwanted physical blade interactions, rotors are locked in alignment about their respective axes through the blade-axis re-enforcing flap adapter (BARFA). The BARFA allows the rotors to push against one-another without touching, and contains the stationary blades responsible for reducing unwanted flow during the sway maneuver. Fig. 14 highlights the BARFA mechanism used in the small-scale model.

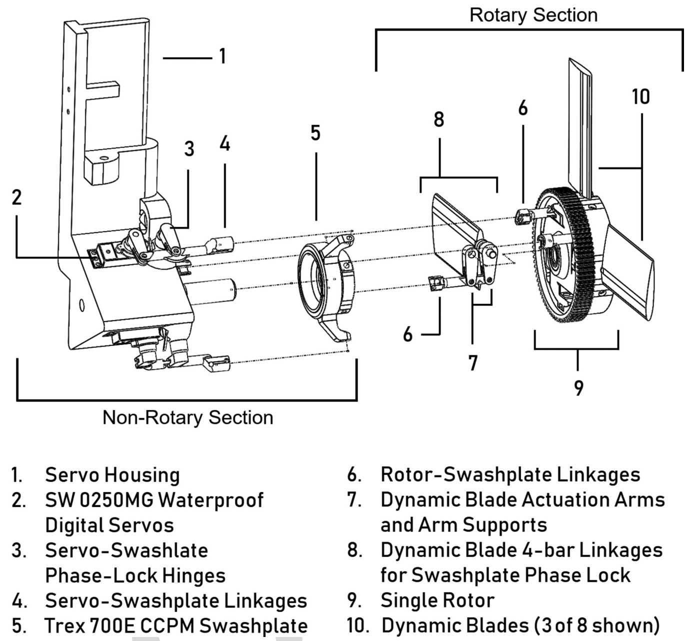

Fig. 15. Small-scale actuation mechanism assembly.

B. Servo-Swashplate Actuation Mechanism

The servo-swashplate actuation mechanism (SSPAM) must quickly and accurately manipulate the pitch of spinning blades in a manner independent of rotation rate, as discussed in Section II. The design consists of two SSPAM assemblies. Each SSPAM links a set of three Savox SW0250MG waterproof servos to four blades through a swashplate mechanism. All blades must remain phase-locked with the swashplate to allow the swashplate to both pull and push on blade pivots. To ensure blade-swashplate phase-alignment, blade pivot arms are arranged as four-bar linkages to lock their alignment with the primary hull axis. Fig. 15 projects an expanded SSPAM assembly in its entirety.

C. Electronic Setup

An economical Arduino-based setup is constructed which routes isolated power to appropriate subsystems while remaining simple and safe to operate. The setup is powered by a 4S LiPo battery feeding directly to the two main ESCs, as well as to three separate Buck converters which independently provide power to the servos and a central Arduino MEGA 2560. Fig. 16 details the electrical layout.

As a first level of safety against a runaway propulsor, the Arduino's throttle command is read from an analog voltage divider that is itself powered by the Arduino. If at any point the analog throttle signal is lost or disconnected while the Arduino is operating correctly, the motors will shut down. As a final level of safety against any malfunction, the setup contains a killswitch pullplug located on the battery's ground lead, which can be pulled from a safe distance to reliably cut power to all systems.

The Arduino reads and reports values from the force-sensing apparatus while also controlling the actuators and brushless

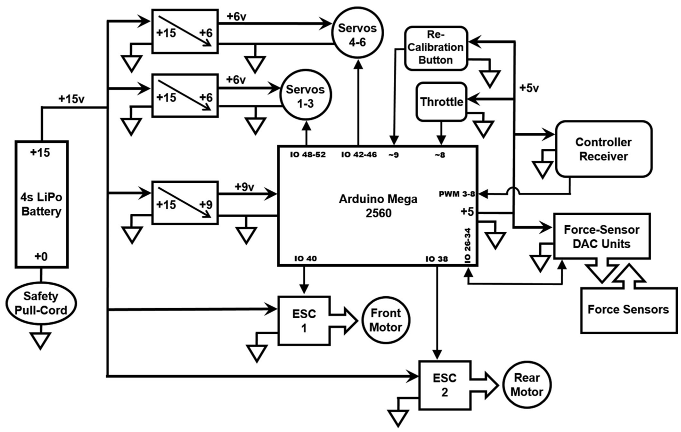

Fig. 16. Layout of electronics used in experimentation.

ESCs. Control mode commands α, Γ_y, Γ_z, δ, β_y, and β_z are interpreted from PWM inputs from an external controller. The Arduino's single-threaded nature prohibits it from simultaneously executing these control mode commands while reading force sensors. Due to the required cool-down time between force-sensor readings, the Arduino's operating loop must update actuator commands every iteration, while only reading from force sensors every fourth iteration. The Arduino then reports the last known sensor readings on iterations between updates. This may cause small illusory input-output delays between control mode commands and sensor readings, but is extremely cost effective- maximizing recorded data with inexpensive hardware. Illusory delays can be upwards of 0.2 s.

IV. Experimental Results and Analysis

At various motor efforts, different control commands are tested and compared against measured forces to gauge the validity of the operating theory. Control commands are physically manifested as pitch changes onto the moving blades. Design geometries ensure that the magnitude of respective pitch change is directly proportional to the magnitude of control command change. For the Wortmann FX 76-100 hydrofoil blade profile used in the mechanism, lift forces generated are linear with blade angle of attack (AoA), hence with pitch and therefore control commands, until around 15^o AoA [18]. Even as the actuators rotate to achieve 15^o pitch, the increasing fluid inflow velocity decreases the effective AoA on the blades. In turn, the linear pitch regime is actually expanded beyond 15^o and is expected to encompass the full operating range of the servos. Control commands may then be pushed well past their normal $(-10^o, 10^o)$ restrictions during signal-maneuver tests, but should still be selectively limited to maintain force-command linearity.

Due to safety concerns, motor effort is never brought past 50% during our study. The brushless motors still operate under some hydrodynamic load, so direct motor effort commands to ESCs are expected to manifest more as torque than speed inputs [19]. Because generated rotor forces are typically linear with torque [20], we can expect forces generated from any particular command to also be linear with motor effort.

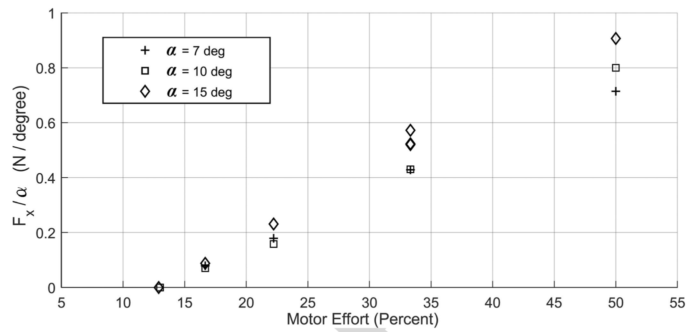

Fig. 17. Surge forces are normalized by α at various motor efforts.

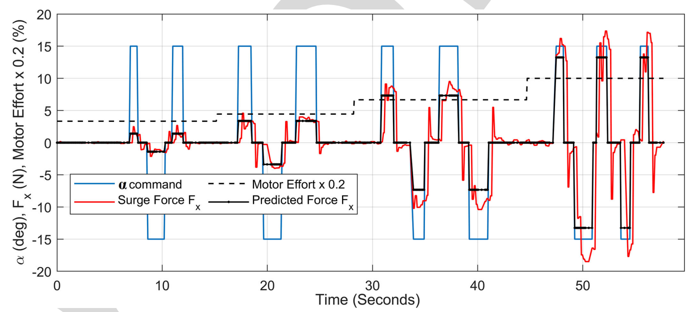

Fig. 18. Pure-surge forces with $\alpha \pm 15^o$ at 16, 22, 33, and 50% motor effort.

A. Pure Surge (α)

The surge-force F_{surge} generated from the surge command α, for example, should then take the form

$$F_{\text{surge}} = K_\alpha(\text{Motor Effort - Motor Offset}) \cdot \alpha \tag{3}$$

where K_α is a scaling factor that links command α to the output force F_{surge} and encompasses all constant unknown hydrodynamic and motor-rate properties. Motor Effort describes the throttle command percent read to the ESCs and imposed on the rotors, while Motor Offset describes the smallest value at which the ESCs actually spin the motors. For the small-scale model, the Motor Offset value is expected to be around 13% effort.

At various motor efforts, different magnitudes of command α are tested and surge forces are recorded. These forces are normalized by their corresponding α commands and plotted against motor effort. To validate the form of (3) and our operating principles as a whole, the plot should reveal a clear linear trend between normalized forces and motor efforts, with an x-axis crossing at around 13% motor effort. Normalized surge forces are plotted against motor effort in Fig. 17.

The surge force model hypothesis is clearly validated in Fig. 17, with $K_\alpha = 2.37\text{E}^{-2}$. We can expect the small-scale propulsor to generate around 32 N thrust at 100% motor effort for surge ($\alpha = 15^o$). For completeness, results from a pure-surge test with 15^o step commands at various motor efforts are presented in Fig. 18.

As explained in Section III-C, perceived delays between input-commands and output-forces in Fig. 18 are illusory and caused primarily by force-sensor update lag. The attached

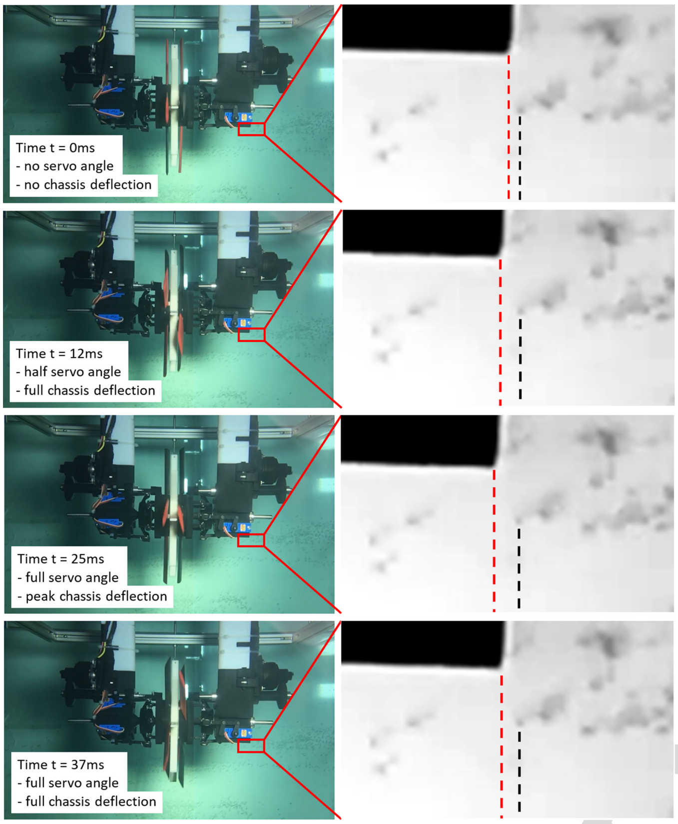

Fig. 19. Slow-motion analysis on chassis deflection for gauging true input-output time delay. Imperfections in testing tank glass are used for relative unitless position.

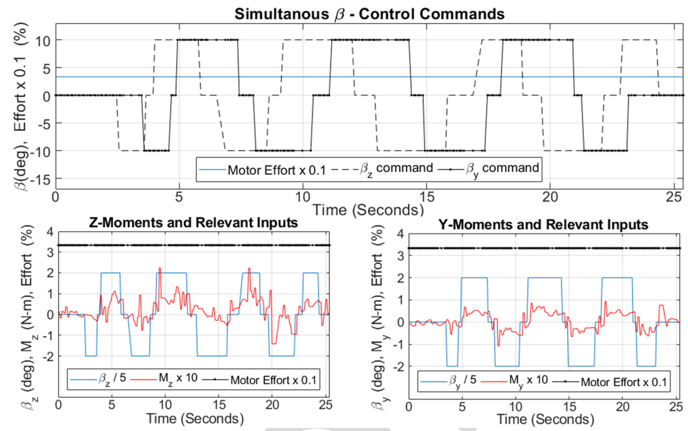

Fig. 20. Simultaneous mixed-yaw forces with $\beta \pm 10^{\mathrm{o}}$.

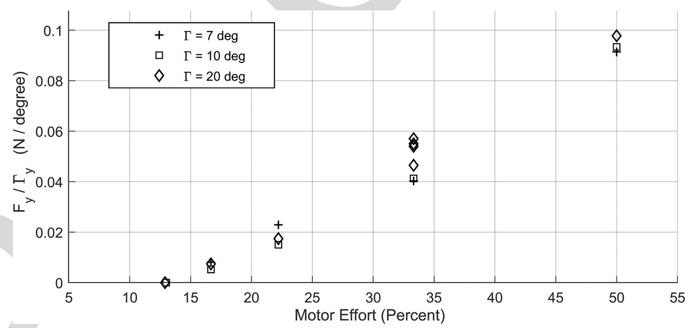

Fig. 21. Sway forces are normalized by Γ at various motor efforts.

propulsor must physically deflect a small amount before the sensors can generate readings, which can be exploited to analyze the propulsor's true reaction time using slow-motion capture. The start time is taken at the instant the servos start moving. Any hydrodynamic force delays are shown to be less than even the 20 ms rise-time of the pitch-actuating servos through slow-motion analysis, as presented in Fig. 19. The deflection of the chassis is understood to coincide directly with actual sensor tension via Hooke's law.

B. Yaw (β)

Both kinematically and hydrodynamically, the yaw maneuver is understood to be very similar to the surge maneuver. While the surge maneuver generates surge force, the yaw maneuver similarly generates yaw moment. The lack of moment-arm due to the limited rotor span on the small-scale model greatly reduces the magnitude of moments measured, but this is understood. For the purposes of this study, the yaw maneuver need only be tested for existence and shown to be decoupled between the two different yaw-axes. Simultaneous β_y and β_z maneuvers are shown to be achievable and decoupled in Fig. 20. The test was conducted with 33% motor effort at β magnitudes of only $\pm 10^{\mathrm{o}}$.

C. Sway (Γ)

One of the primary objectives of this study is to gauge the validity of the novel sway maneuver principle. Our current model assumes the force response to sway behaves in a similar manner to surge. Like surge, the sway-force F_{sway} generated from sway command Γ should scale as

$$F_{\mathrm{sway}} = K_{\Gamma}(\text{Motor Effort - Motor Offset}) \cdot \Gamma \qquad (4)$$

where K_{Γ} is a scaling factor which links sway-command Γ to the output force F_{sway} and encompasses all constant unknown hydrodynamic and motor-rate properties. For the small-scale model, the *offset* value is expected to be around 13% effort.

At various motor efforts, different magnitudes of command Γ_{y} are tested and sway forces F_{y} are recorded. These forces are normalized by their corresponding Γ_{y} commands and plotted against motor effort. To validate the form of (4) and our operating principles as a whole, the plot should reveal a clear linear trend between normalized forces and motor efforts, with an x-axis crossing at around 13% motor effort. Normalized sway forces are plotted against motor effort in Fig. 21.

The sway force model hypothesis is clearly validated in Fig. 20, with $K_{\Gamma} = 2.67\mathrm{E}^{-3}$. The model predicts the small-scale propulsor to generate around 4.6 N at 100% motor effort for sway ($\Gamma = 20^{\mathrm{o}}$). For completeness, results from a pure-sway test

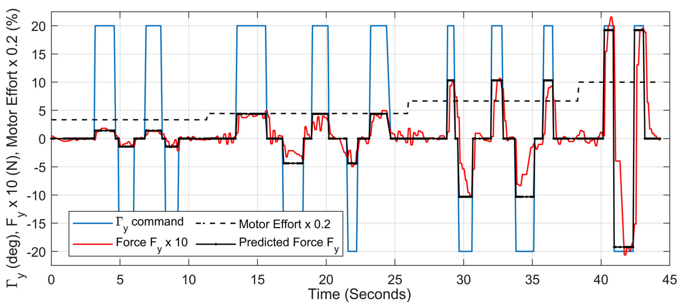

Fig. 22. Pure-sway forces with $\Gamma_y \pm 20^o$ at 16, 22, 33, and 50% motor effort.

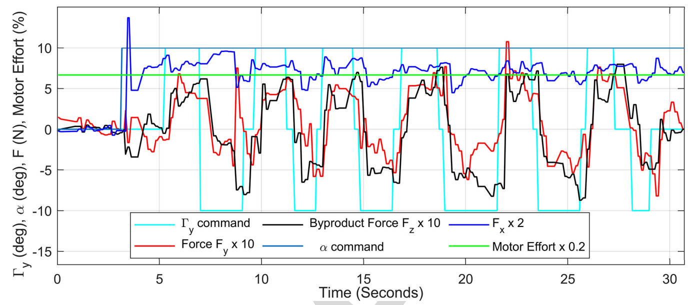

Fig. 24. Cross-planar lateral-force coupling through simultaneous Γ and α commands.

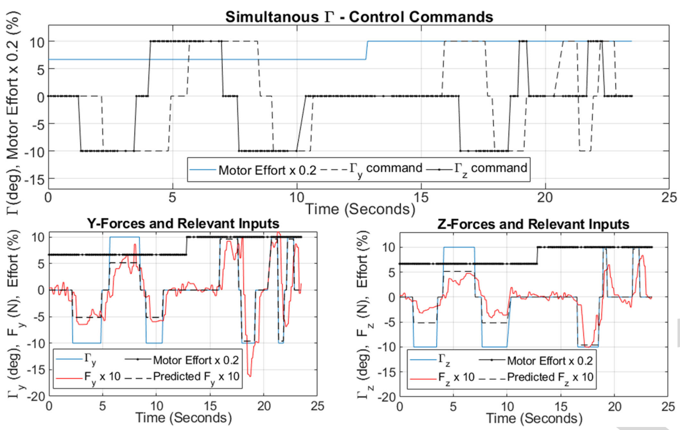

Fig. 23. Simultaneous mixed-sway forces with $\Gamma \pm 10^o$.

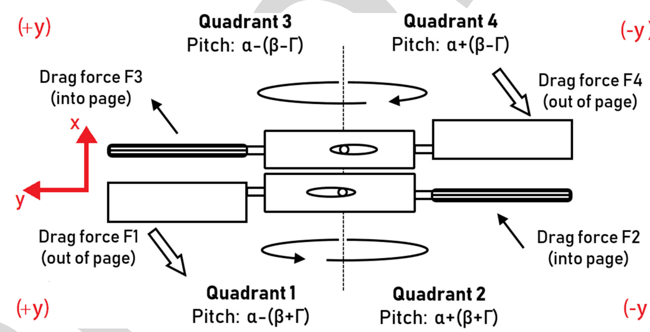

Fig. 25. 2-D representation of final blade angles with resulting drag forces.

with 20° step commands at various motor efforts are presented in Fig. 22.

Simultaneous Γ_y and Γ_z maneuvers are shown to be achievable and decoupled in Fig. 23. The test was conducted with 33% and 50% motor effort at Γ-command magnitudes of only $\pm 10^o$.

D. Control-Command Interactions

Control command combinations (α, β), and (β, Γ) are tested and confirmed to be decoupled. Testing of the combination (α, Γ) reveals some cross-planar coupling, which can be explained through blade drag analysis and then compensated for in a straightforward manner. Forces from an $\alpha + \Gamma$ test are presented in Fig. 24 which shows the unwanted cross-planar interference.

E. Compensation for $\alpha + \Gamma$ Cross-Planar Coupling

Drag-forces on rotating blades can induce coupling between maneuvers on separate planes. Returning to the 2-D planar representation of blade angles from Fig. 6, Fig. 25 presents the total pitches of blades as they pass through four quadrants, as well as their respective drag forces into or out of the page. Blade drag projected from the xy-plane manifests as an unwanted sway force in the xz-plane.

The total drag force into or out of the page is calculated with the understanding that drag scales with pitch angle *squared* [18]. The total force into the page is then

$$\begin{aligned} F_{\text{tangential plane}} &= (F_2 - F_1) - (F_4 - F_3) \\ &\propto \big((\alpha+(\beta+\Gamma))^2-(\alpha-(\beta+\Gamma))^2\big)-\big((\alpha+(\beta-\Gamma))^2-(\alpha-(\beta-\Gamma))^2\big)= 8\alpha\Gamma \\ &\propto \alpha\Gamma \end{aligned} \tag{5}$$

where the β command cancels out, ensuring that any unwanted cross-planar force is proportional only to the product of commands α and Γ and is independent of β.

It is possible to compensate for this unwanted cross-planar sway force through a Γ-sway command in the other plane. Recall that the command α is shared across all servos in both planes and motor effort is also shared everywhere. Any desired sway force $F_{\text{wanted}} = K_1\Gamma$ in one plane generates an unwanted byproduct sway force $F_{\text{unwanted}} = K_2\alpha\Gamma$ in the other. So long as the ratio between unwanted byproduct force and desired force $\frac{K_2\alpha\Gamma}{K_1\Gamma} \triangleq K_3\alpha$ is known, cross-planar coupling can be compensated for straightforwardly. The compensation process actually amplifies the desired sway forces generated, because the coupling only alters the effective direction of applied sway force while increasing its magnitude. For any desired commands $\Gamma_{\text{y, des}}$, $\Gamma_{\text{z, des}}$, and α, the final compensated sway commands $\Gamma_{\text{y, fin}}$ and, $\Gamma_{\text{z, fin}}$ are derived through a system of equations linking the two planes

$$\left.\begin{aligned} K_1\Gamma_{\text{y, fin}} - K_2\alpha\Gamma_{\text{z, fin}} &= K_1\Gamma_{\text{y, des}} \\ K_1\Gamma_{\text{z, fin}} + K_2\alpha\Gamma_{\text{y, fin}} &= K_1\Gamma_{\text{z, des}} \end{aligned}\right\} \begin{aligned} \Gamma_{\text{y, fin}} &= \frac{\Gamma_{\text{y, des}} + K_3\alpha\Gamma_{\text{z, des}}}{1+(K_3\alpha)^2} \\ \Gamma_{\text{z, fin}} &= \frac{\Gamma_{\text{z, des}} - K_3\alpha\Gamma_{\text{y, des}}}{1+(K_3\alpha)^2} \end{aligned} \tag{6}$$

effectively decoupling the two axes and eliminating cross-planar interference. From Fig. 24, K_3 is approximately $0.1\frac{N}{(N-deg\alpha)}$. Final commands $\Gamma_{\text{y, fin}}$ and $\Gamma_{\text{z, fin}}$ are read directly to actuators through (2). Desired commands $\Gamma_{\text{y, des}}$ and $\Gamma_{\text{z, des}}$ are used for control and will be referred to as Γ_{y} and Γ_{z}, respectively.

For the small-scale model operating at 50% motor effort, open-loop control parameters are mapped to forces and torques as follows:

$$\begin{bmatrix} F_x \\ F_{\text{y}} \\ F_{\text{z}} \\ T_x \\ T_{\text{y}} \\ T_{\text{z}} \end{bmatrix} = \begin{bmatrix} F_{\text{surge}} \\ F_{\text{sway}} \\ F_{\text{heave}} \\ T_{\text{roll}} \\ T_{\text{pitch}} \\ T_{\text{yaw}} \end{bmatrix} = \begin{bmatrix} 8.9\text{E}^{-1} & 0 & 0 & 0 & 0 & 0 \\ 0 & 9.6\text{E}^{-2} & 0 & 0 & 0 & 0 \\ 0 & 0 & 9.6\text{E}^{-2} & 0 & 0 & 0 \\ 0 & 0 & 0 & 7.1\text{E}^{-4} & 0 & 0 \\ 0 & 0 & 0 & 0 & 2.2\text{E}^{-2} & 0 \\ 0 & 0 & 0 & 0 & 0 & 2.2\text{E}^{-2} \end{bmatrix} \begin{bmatrix} \alpha \\ \Gamma_{\text{y}} \\ \Gamma_{\text{z}} \\ \delta \\ \beta_{\text{y}} \\ \beta_{\text{z}} \end{bmatrix}. \tag{7}$$

V. Conclusion

This article validates the underlying concepts behind an omnidirectional vehicle with speed and agility sufficient enough to work in turbulent environments inaccessible to traditional craft, as would be seen in many shallow marine environments that require inspection. The propulsor exploits properties emerging from continuous counter-rotating blades to generate near-instantaneous forces and moments in six degrees of freedom of considerable magnitude, and is designed to allow each DOF to be controlled independently by one of six decoupled control parameters. In this study, a small-scale model is built to verify different sets of maneuvers that would be used in the full-scale model. Slow-motion analysis confirms the instantaneous reaction time. Our novel method to generate lateral sway force underwater was originally simulated using STARCCM+ CFD software. Simulations suggested that the propulsor could generate sway thrust at a magnitude near 10–20% surge thrust capability [6], which was validated through the small-scale physical tests presented in this study.

A straightforward method for reorienting lateral forces resulting from blade drag was presented, and a basic open-loop controller was designed linking all open-loop control parameters for surge, yaw, and roll to desired output forces and moments on the small-scale model. We have shown that omnidirectional ROV propulsion can be achieved through a fully actuated counter-rotating blade mechanism to potential speeds well beyond anything achieved through traditional ROV thrusters [21], and have validated the feasibility of producing instantaneous sway force using this mechanism.

Our conceptual validation of the agile omnidirectional mechanism calls for future work on the system, including simulation or experimentation of closed-loop, inertia-based feedback performance to gauge rejection of heavy external fluid disturbances. Details regarding operating characteristics of the force-sensing apparatus and physical implementation of the sway-force re-alignment algorithm (6) are also reserved for future work.

References

[1] Y. Shi, C. Shen, H. Fang, and H. Li, "Advanced control in marine mechatronic systems: A survey," *IEEE/ASME Trans. Mechatronics*, vol. 22, no. 3, pp. 1121–1131, Jun. 2017.

[2] K. Tanakitkorn, P. A. Wilson, S. R. Turnock, and A. B. Phillips, "Depth control for an over-actuated, hover-capable autonomous underwater vehicle with experimental verification," *Mechatronics*, vol. 41, pp. 67–81, 2017. [Online]. Available: http://dx.doi.org/10.1016/j.mechatronics.2016.11.006

[3] A. Mazumdar and H. H. Asada, "Control-configured design of spheroidal, appendage-free, underwater vehicles," *IEEE Trans. Robot.*, vol. 30, no. 2, pp. 448–460, Apr. 2014.

[4] Y. Yang, Z. Fan, Z. Zhu, and J. Zhang, "Underwater modeling, experiments and control strategies of FroBot," in *Proc. IEEE Int. Conf. Intell. Robots Syst.*, Oct. 2018, pp. 6397–6403.

[5] O. Chocron, U. Prieur, and L. Pino, "A validated feasibility prototype for AUV reconfigurable magnetic coupling thruster," *IEEE/ASME Trans. Mechatronics*, vol. 19, no. 2, pp. 642–650, Apr. 2014.

[6] T. Njaka, S. Brizzolara, and P. Ben-Tzvi, "Design and simulation of a fully-actuated underwater propulsion mechanism," in *Proc. Amer. Soc. Mech. Engineers*, Anaheim, CA, USA, 2019, Art. no. 97534.

[7] C. A. Goudey, T. R. Consi, J. W. Bales, D. K. Atwood, J. J. Leonard, and C. Chryssostomidis, "A second generation survey AUV," in *Proc. Auton. Underwater Vehicle*, 1994, pp. 148–155.

[8] "Media downloads | oceana subsea independent ROV services," [Online]. Available: http://www.oceanasubsea.com/media-downloads

[9] R. H. Maloof, N. C. Forrester, and C. E. Albrecht, "A brushless electric propulsion system for the research submersible alvin," in *Proc. IEEE/Mar. Technol. Soc. Oceans*, 1986. Q2

[10] R. Wernli, "The present and future capabilities of deep ROVs," *Mar. Technol. Soc. J.*, vol. 33, no. 4, pp. 26–40, 1999. [Online]. Available: http://openurl.ingenta.com/content/xref?genre=article&issn=0025-3324&volume=33&issue=4&spage=26

[11] O. A. Eidsvik and I. Schjølberg, "Determination of hydrodynamic parameters for remotely operated vehicles," in *Proc. Int. Conf. Ocean Artic Eng.*, Oct. 2016. [Online]. Available: http://proceedings.asmedigitalcollection.asme.org/proceeding.aspx?doi=1 0.1115/OMAE2016-54642

[12] M. E. Kepler, S. Pawar, D. J. Stilwell, S. Brizzolara, and W. L. Neu, "Assessment of AUV hydrodynamic coefficients from analytic and semi-empirical methods," in *Proc. OCEANS*, Oct. 2018.

[13] T. Njaka, S. Brizzolara, and D. Stilwell, "CFD investigation of hull-rudder interaction for improved maneuvering models," in *Proc. Soc. Nav. Architects Mar. Eng. Mar. Conv.*, Oct. 2019.

[14] L. Chikh, *MEROS Project Technical Advances in Modeling and Control*, Feb. 2013. Q3

[15] J. G. Leishman, *Principles of Helicopter Aerodynamics*, 2nd ed. New York, NY, USA: Cambridge University Press, 2006. [Online]. Available: https://www.worldcat.org/title/principles-of-helicopter-aerodynamics/oc lc/886667957

[16] C. N. Eastwick and G. Johnson, "Gear windage: A review," *J. Mech. Des. Trans. Amer. Soc. Mech. Eng.*, vol. 130, no. 3, pp. 1–6, 2008.

[17] F. Concli, C. Gorla, A. D. Torre, and G. Montenegro, "Windage power losses of ordinary gears: Different CFD approaches aimed to the reduction of the computational effort," *Lubricants*, vol. 2, no. 4, pp. 162–176, 2014.

[18] WORTMANN, "WORTMANN FX 76-100 (fx76100-il)," [Online]. Available: http://airfoiltools.com/airfoil/details?airfoil=fx76100-il Q4

[19] J. C. Gamazo-Real, E. Vázquez-Sánchez, and J. Gómez-Gil, "Position and speed control of brushless dc motors using sensorless techniques and application trends," *Sensors*, vol. 10, no. 7, pp. 6901–6947, 2010.

[20] H. K. Woud and D. Stapersma, "Chapter 3 Propulsion and Electric Power," in *Design of Propulsion and Electric Power Generation Systems*. London, U.K.: IMarEST, 2002, ch. 3.

[21] AKVA, "World's fastest ROV? - Project ROST," 2018. [Online]. Available: https://www.akvagroup.com/news/news-archive/news-view/world-s-fastest-r ov-project-rost

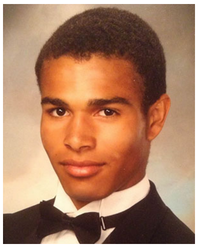

Taylor Njaka (Graduate Student Member, IEEE) received the B.S. degree in mechanical and ocean engineering from the Massachusetts Institute of Technology, Cambridge, MA, USA, in 2017. He is currently working toward the Ph.D. degree in mechanical engineering from the Robotics and Mechatronics Laboratory, Virginia Tech, Blacksburg, VA, USA, where he also works under the VT iSHIP Laboratory and the Center for Marine Robotics and Autonomy.

His research interests include underwater robotics and mechatronics, along with dynamic system identification and modeling of unmanned underwater vehicles.

Stefano Brizzolara received the B.S. and M.S. degrees (*summa cum laude*) from the University of Genoa, Italy, in 1994, both in naval architecture and marine engineering and the Ph.D. in naval architecture from the University Federico II, Naples, Italy in 2000.

He is currently an Associate Professor and the Director and Founder of the VT iShip lab at the Kevin Crofton Department of Aerospace and Ocean Engineering, Virginia Tech, and Associate Director of the Center of Marine Autonomy and Robotics. He has been a Peabody Visiting Associate Professor in the MIT dept. of Mechanical Engineering. His research interests include CFD, design of advanced marine underwater and surface vehicles, design of high performance marine propulsors, and numerical hydrodynamics for ship design.

Dr. Brizzolara is an Associate Editor for the *SMAME Journal of Ship Research*, and a Board Member on the *RINA Int'l Journal of Maritime Engineering*, the *RINA Int'l Journal of Small Craft Technology*, and the Springer Journal of Marine Science and Application. He has received the 2018 Calder Prize for Best Paper on the subject of high speed crafts, the 2016 Excellence in Review for the *IEEE Journal of Oceanic Engineering*, and the 2015 Mandel's Prize for Excellence in Hydrofoil Research advising.

Pinhas Ben-Tzvi (Senior Member, IEEE) received the B.S. degree (*summa cum laude*) from the Technion—Israel Institute of Technology, Israel, and the M.S. and Ph.D. degrees from the University of Toronto, Canada, all in mechanical engineering.

He is currently a Professor of mechanical engineering and electrical and computer engineering, and the founding Director of the Robotics and Mechatronics Laboratory with Virginia Tech, Blacksburg, VA, USA. His current research interests include robotics and intelligent autonomous systems, human-robot interactions, robotic vision and visual servoing/odometry, machine learning, mechatronics design, systems dynamics and control, mechanism design and system integration, and novel sensing and actuation.

Dr. Ben-Tzvi is the Recipient of the 2019 Virginia Tech Excellence in Teaching Award, 2018 Virginia Tech Faculty Fellow Award, the 2013 GWU SEAS Outstanding Young Researcher and Outstanding Young Teacher Awards, as well as several other honors and awards. He is a Technical Editor for the IEEE/ASME TRANSACTIONS ON MECHATRONICS, Associate Editor for *ASME Journal of Mechanisms and Robotics*, Associate Editor for IEEE Robotics and Automation Magazine, and an Associate Editor for the *Int'l Journal of Control, Automation and Systems* and served as an Associate Editor for IEEE ICRA 2013- 2018. He is a Member of the American Society of Mechanical Engineers (ASME).